Analysis of a Vibrating Interventional Device to Improve 3-D Colormark Tracking

Matthew P. Fronheiser and Stephen W. Smith, *Member, IEEE*

***Abstract*—Ultrasound guidance of interventional devices during minimally invasive surgical procedures has been investigated by many researchers. Previously, we extended the methods used by the Colormark tracking system to several interventional devices using a real-time, three-dimensional (3-D) ultrasound system. These results showed that we needed to improve the efficiency and reliability of the tracking. In this paper, we describe an analytical model to predict the transverse vibrations along the length of an atrial septal puncture needle to enable design improvements of the tracking system. We assume the needle can be modeled as a hollow bar with a circular cross section with a fixed proximal end and a free distal end that is suspended vertically to ignore gravity effects. The initial results show an ability to predict the natural nodes and antinodes along the needle using the characteristic equation for free vibrations. Simulations show that applying a forcing function to the device at a natural antinode yields an order of magnitude larger vibration than when driving the device at a node. Pulsed wave spectral Doppler data was acquired along the distal portion of the needle in a water tank using a 2-D matrix array transesophageal echocardiography probe. This data was compared to simulations of forced vibrations from the model. These initial results suggest that the model is a good first order approximation of the vibrating device in a water tank. It is our belief that knowing the location of the natural nodes and antinodes will improve our ability to drive the device to ensure the vibrations at the proximal end will reach the tip of the device, which in turn should improve our ability to track the device *in vivo*.**

I. Introduction

Ultrasonic image guidance during minimally invasive surgical procedures provides the clinician with excellent soft tissue contrast without ionizing radiation, but there is often a problem identifying the interventional devices as they tend to be specular reflectors that do not return the ultrasonic echoes back toward the transducer. There have been many techniques used to improve the visualization of the devices. One way to improve device visualization is to modify the devices by adding an echogenic coating or by scoring, etching, or dimpling, all of which improve the backscatter from the device. Studies have shown that making such modifications can increase visualization of the treated device when compared to a similar untreated device [1]–[4]. Despite this improved visualization, tip localization is not necessarily improved in all cases. Other researchers have attempted to track catheters by attaching sensors that interact with the ultrasound beam. One such commercial system, the EchoMark (EchoCath, Princeton, NJ), used an omni directional receiver that was positioned at a key point on the catheter to receive ultrasonic energy [5], [6]. Researchers at Duke expanded on this idea by attaching a receiver to the tip of a catheter and imaged the device with a real-time, three-dimensional (RT3D) ultrasound system [7]. Both of these systems produced accurate results. But attaching a sensor to the tip of a catheter increases the cost of the device and could create safety issues.

Alternative guidance techniques have focused on using color Doppler techniques to track interventional devices. The first methods involved a passive technique, also known as the pump technique, in which biopsy needles or guidewires were repeatedly advanced and retracted. Although effective, again tip identification is not always clear, and the signal is present only when the device is being manipulated [8]. Armstrong *et al.* [9] used a Food and Drug Administration (FDA) approved commercial device, the ColorMark (Echocath, Princeton, NJ), to couple low frequency vibrations (1–3 kHz) into an aspiration needle. These vibrations were detected and displayed with the color Doppler feature of a B-scan system in a clinical trial applied to pericardiocentesis. Despite positive results in both *in vitro* and *in vivo* experiments, it is noteworthy that the authors recognized the limitation of the planar nature of the 2-D ultrasound beam. We have implemented this method for real-time detection and guidance of minimally invasive devices using RT3D ultrasound [10], [11].

The Model 1 RT3D ultrasound system (Volumetrics Medical Imaging, Durham, NC), originally developed at Duke University [12], [13], has been used to address the inherent limitations associated with device tracking using conventional 2-D imaging techniques such as monoplane ultrasound. The 3-D system uses up to 512 transmitters and 256 receive channels, and also uses 16:1 receive mode parallel receive processing to generate 4096 B-mode image lines at up to 30 volumes per second. From the pyramidal volume of echo data, the scanner displays two simultaneous orthogonal B-mode image planes and up to three C-mode planes parallel to the array face (Fig. 1). Each image plane can be inclined at any desired angle. By integrating and spatially filtering between two user-selected, parallel C-mode planes, the system can display real-time, 3-D rendered images. The system offers both 3-D pulsed wave (PW) spectral Doppler and 3-D color Doppler features over the complete pyramid. During the past few years, RT3D echocardiography has been introduced by several other manufacturers, and its clinical use is growing rapidly.

Manuscript received August 14, 2006; accepted March 13, 2007.

The authors are with the Department of Biomedical Engineering, Duke University, Durham, NC (e-mail: mpf3@duke.edu).

Digital Object Identifier 10.1109/TUFFC.2007.442

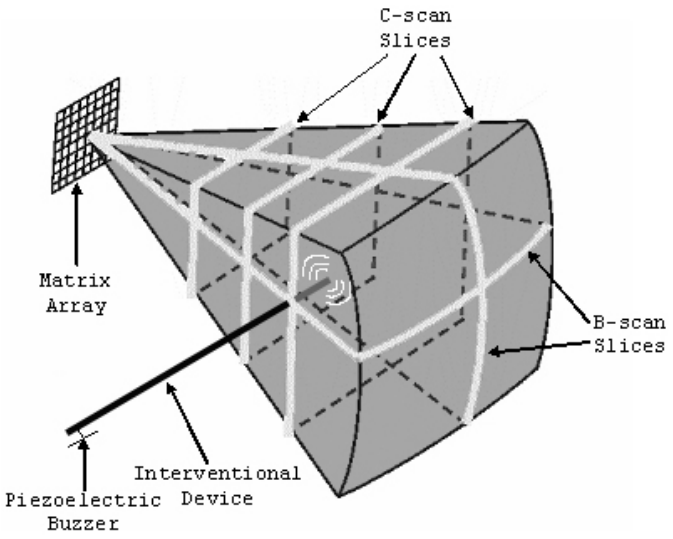

Fig. 1. Schematic of pyramidal scan showing the scanned volume of echo data generated by the matrix array and the orthogonal B-scans and C-scans slices.

In our previous work [10], several experiments were performed using four different interventional devices that were modified by attaching a unimorph piezoelectric actuator to couple 0.5–8 kHz vibrations to each interventional device. The piezoelectric buzzer was driven using a function generator and an audio amplifier. As illustrated in Fig. 1, these vibrations were coupled into the device, causing deflections along the length of the device. When the vibrating tip was inserted into the 3-D pyramidal scan created by the matrix array, signals from the vibrating device were acquired and sent to the 3-D scanner for Doppler processing before being displayed. The devices and sample experimental color Doppler image slices from volumetric scans are presented in the previous work [10].

Notwithstanding these positive results, our experiments have shown limitations with reliability and consistent device tip detection during the *in vivo* experiments. We believe that modeling the intervention devices to characterize the vibrations along the length of the vibrating device will enable design improvements in the tracking system. Gardineer and Bogan [14] previously modeled the vibrating tip of a biopsy needle by creating a 3-D model using finite-element analysis software. This model of the needle tip was used to find the optimal frequency for the piezoelectric driver. The results showed a series of different frequency bands that represented the preferred ranges to drive the piezoelectric buzzer. However, no results were presented for vibrations along the length of the needle.

In this paper, an analytical model is presented to simulate the vibration of the atrial septal puncture needle, which was one of the devices used in our previous work [10]. The first goal of the model is to help predict the location of the natural nodes and antinodes along the needle length. This will allow the piezeoelectric buzzer to be placed near a natural antinode for a particular driving frequency to maximize the vibration amplitude at the tip. During *in vitro* experiments, we measured a threshold associated with the drive amplitude that must be surpassed before we are able to detect the needle tip with color Doppler. As the drive amplitude increases, increasing the amplitude of vibration, the color dot signifying the needle tip continues to grow. From this observation, we conclude that placing the buzzer near a natural antinode will have the same effect as increasing the drive amplitude delivered to the buzzer. This increased vibration amplitude should enable us to better detect the vibrating needle during *in vivo* experiments.

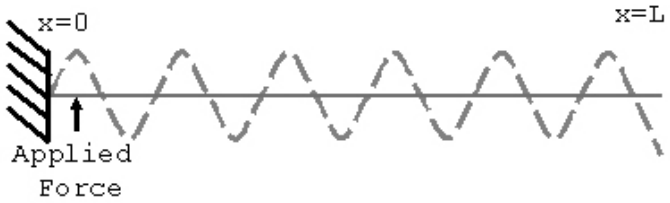

Fig. 2. Schematic showing the boundary conditions for the current model. The left side of the device is fixed, and the right side is left free. A force is applied (when applicable) toward the proximal end of the device. The resulting vibrations are shown by the dashed line.

The model also will enable a node to be placed at the location at which the needle enters the introducer catheter to minimize vibration damping at this insertion point, again to ensure maximum vibration at the tip. In the future, the model could be used to predict the vibration amplitude at the tip for a variety of frequencies. This would enable us to select the frequency that provides the largest transverse deflections at the needle tip to improve visualization. Also, the model could be used for other vibrating interventional devices by changing the device geometry and material properties.

II. Methods

A. Analytical Model

Our model was created by modifying the derivation previously described for a vibrating beam to the case of a hollow rod [15]. The schematic in Fig. 2 shows the boundary conditions and assumptions. Our model assumes the needle can be represented as a hollow beam that is fixed at the proximal end, free at the distal end, and has a constant cross-sectional area and moment of inertia. Also, it is assumed that the beam is in the vertical position to eliminate the distributed load effects caused by gravity on a cantilever. From these assumptions, the needle's transverse displacement can be represented by:

$$EI\frac{\partial^4 w(x,t)}{\partial x^4} = p(x,t) - \rho\Omega\frac{\partial^2 w(x,t)}{\partial t^2}, \qquad (1)$$

where E is Young's modulus, I is the moment of inertia of mass, $w(x,t)$ is the transverse displacement, x is the location along the needle, $p(x,t)$ is an external force, ρ is the mass density of the material, Ω is the cross-section area, and t is time. First, the free vibration case will be

examined to solve for the characteristic functions. These functions will be used to find the natural nodes and antinodes along the length of the needle for a given frequency and to solve for the forced vibration case.

To solve for the characteristic functions, the free vibration case, where $p(x,t)$ is set to zero, is examined. The free vibration case can be solved using the method of separation of variables by assuming that $w(x,t) = X(x)f(t)$, which, when substituted into (1), yields two ordinary differential equations satisfied by $X(x)$ and $f(t)$:

$$\frac{\partial^2 f(t)}{\partial t^2} + \omega^2 f(t) = 0, \tag{2}$$

$$\frac{\partial^4 X(x)}{\partial x^4} - k^4 X(x) = 0, \tag{3}$$

where ω is a separation of variables constant and $k^2 = \sqrt{(\omega^2 \rho \Omega / EI)}$. The general solution for (2) is:

$$f(t) = A\cos(\omega t) + B\sin(\omega t). \tag{4}$$

The coefficients A and B depend on the initial transverse displacement and transverse velocity, respectively. We assume that the needle begins at rest along the entire length, resulting in initial displacement and velocity values of zero. This assumption causes the coefficients A and B to equal zero, which then causes the function $f(t)$ to equal zero, yielding no free vibrations.

The characteristic functions, which are used to find the modal shapes of the device, can be derived from the general solution for (3), which can be expressed as follows [15]:

$$\begin{aligned} X(x) = {} & C_1\left[\cos(kx) + \frac{e^{k(x-L)} + e^{-kx}}{2}\right] \\ & + C_2\left[\cos(kx) - \frac{e^{k(x-L)} + e^{-kx}}{2}\right] \\ & + C_3\left[\sin(kx) + \frac{e^{k(x-L)} - e^{-kx}}{2}\right] \\ & + C_4\left[\sin(kx) + \frac{e^{k(x-L)} - e^{-kx}}{2}\right]. \end{aligned} \tag{5}$$

The constants C_1, C_2, C_3, and C_4 for each modal shape can be found by applying the boundary conditions. For the case of the fixed-free hollow bar with a length L, the boundary conditions are:

$$\begin{aligned} & w(0,t) = 0; \quad \tfrac{\partial w}{\partial x}(0,t) = 0 \\ & \qquad\qquad\qquad\qquad \text{for } t \geq 0. \\ & \tfrac{\partial^2 w}{\partial x^2}(L,t) = 0; \ \tfrac{\partial^3 w}{\partial x^3}(L,t) = 0 \end{aligned} \tag{6}$$

These boundary conditions lead to the following frequency equation:

$$\begin{aligned} & -e^{-kL} - \cos(kL) - e^{-2kL}\cos(kL) \\ & \qquad - e^{-kL}\cos(kL)^2 - e^{-kL}\sin(kL)^2 = 0. \end{aligned} \tag{7}$$

There are multiple roots for (7), which can be used to solve for the characteristic (natural) frequencies:

$$\omega_n = k^2 n \sqrt{\frac{EI}{\rho\Omega}} = k^2 n \cdot \kappa \cdot c, \tag{8}$$

where κ is the radius of gyration of the cross-sectional area and c is the longitudinal speed of sound in the material. Each characteristic frequency has a characteristic function from (5):

$$\begin{aligned} X_n(x) = {} & C_{1n}\left[\cos(k_n x) + \frac{e^{k_n(x-L)} + e^{-k_n x}}{2}\right] \\ & + C_{2n}\left[\cos(k_n x) - \frac{e^{k_n(x-L)} + e^{-k_n x}}{2}\right] \\ & + C_{3n}\left[\sin(k_n x) + \frac{e^{k_n(x-L)} - e^{-k_n x}}{2}\right] \\ & + C_4\left[\sin(k_n x) + \frac{e^{k_n(x-L)} - e^{-k_n x}}{2}\right]. \end{aligned} \tag{9}$$

The constants C_{1n}, C_{2n}, C_{3n}, and C_{4n} were found using the boundary conditions in (6), creating four equations that were used to solve for the four unknowns. These unknowns were found using substitution methods with the aid of the Mathmatica software (Wolfram Research Inc., Champaign, IL) and are shown in (10) (see next page).

This model also will be used to examine the vibrations along the needle length while a time-varying forcing function is applied near the proximal end of the needle. The general solution for this case is:

$$\begin{aligned} w(x,t) = \sum_{n=1}^{\infty} \Bigg[& A_n\cos(\omega_n t) + B_n\sin(\omega_n t) \\ & + \frac{2}{\rho\Omega L\omega_n}\int_0^t Q_n(\tau)\sin(\omega_n(t-\tau)d\tau)\Bigg] X_n(x), \end{aligned} \tag{11}$$

for

$$Q_n(t) = \int_0^L p(x,t)X_n(x)dx, \tag{12}$$

where $p(x,t)$ is the external force [15]. The first two terms for this equation concern the free vibrations case, which can be ignored because the needle is assumed to start with no initial displacement or velocity, resulting in the coefficients A and B equaling zero. To test the model, the external force was assumed to be a time-varying sinusoidal function placed at one specific location. This assumption sets $p(a,t) = P_o\sin(\omega_{\text{drive}}t)$, where a is the location of the applied forcing function, P_o is the amplitude of the forcing function, ω_{drive} is the driving frequency ($2\pi f_{\text{drive}}$), and t is time. Substituting this into (12) yields:

$$Q_n(t) = P_o\sin(\omega_{\text{drive}}t)\,X_n(a). \tag{13}$$

Substituting (9) and (13) into (11) yields the solution for the transverse motion:

$$\begin{aligned} & w(x,t) = \\ & \sum_{n=1}^{\infty}\left[\frac{2P_o}{\rho\Omega L\omega_n}X_n(a)\frac{\omega_{\text{drive}}\sin(\omega_n t) - \omega_n\sin(\omega_{\text{drive}}t)}{\omega_{\text{drive}}^2 - \omega_n^2}\right] \\ & \qquad\qquad \times X_n(x). \end{aligned} \tag{14}$$

$$
\begin{aligned}
C_{1n} &= -\Big[2e^{k_nL} + \cos(k_nL) + e^{k_nL}\cos(k_nL) + 2e^{2k_nL}\cos(k_nL) + e^{k_nL}\cos^2(k_nL) + e^{2k_nL}\cos^2(k_nL) + \sin(k_nL) \\
&\quad - e^{k_nL}\sin(k_nL) + e^{k_nL}\sin^2(k_nL) + e^{k_nL}\sin^2(k_nL) + e^{k_nL}\sin^2(k_nL) + e^{2k_nL}\sin^2(k_nL)\Big] \Big/ \Big[\cos(k_nL) \\
&\quad + e^{k_nL}\cos(k_nL) - 2e^{2k_nL}\cos(k_nL) - e^{k_nL}\cos^2(k_nL) + e^{2k_nL}\cos^2(k_nL) - \sin(k_nL) - e^{k_nL}\sin(k_nL) \\
&\quad - 2e^{2k_nL}\sin(k_nL) - e^{k_nL}\sin^2(k_nL) + e^{2k_nL}\sin^2(k_nL)\Big] \\
C_{2n} &= \Big[-2e^{k_nL} - \cos(k_nL) + e^{k_nL}\cos(k_nL) + e^{k_nL}\cos^2(k_nL) + e^{2k_nL}\cos^2(k_nL) - \sin(k_nL) - e^{k_nL}\sin(k_nL) \\
&\quad + 2e^{2k_nL}\sin(k_nL) + e^{k_nL}\sin^2(k_nL) + e^{2k_nL}\sin^2(k_nL)\Big] \Big/ \Big[\cos(k_nL) + e^{k_nL}\cos(k_nL) - 2e^{2k_nL}\cos(k_nL) \\
&\quad - e^{k_nL}\cos^2(k_nL) + e^{2k_nL}\cos^2(k_nL) - \sin(k_nL) - e^{k_nL}\sin(k_nL) - 2e^{2k_nL}\sin(k_nL) - e^{k_nL}\sin^2(k_nL) \\
&\quad + e^{2k_nL}\sin^2(k_nL)\Big] \\
C_{3n} &= -\Big[\left(-1 + e^{k_nL}\right)\left(\cos(k_nL) + e^{k_nL}\cos^2(k_nL) - \sin(k_nL) + e^{k_nL}\sin^2(k_nL)\right)\Big] \Big/ \Big[\cos(k_nL) + e^{k_nL}\cos(k_nL) \\
&\quad - 2e^{2k_nL}\cos(k_nL) - e^{k_nL}\cos^2(k_nL) + e^{2k_nL}\cos^2(k_nL) - \sin(k_nL) - e^{k_nL}\sin(k_nL) - 2e^{2k_nL}\sin(k_nL) \\
&\quad - e^{k_nL}\sin^2(k_nL) + e^{2k_nL}\sin^2(k_nL)\Big] \\
C_{4n} &= 1
\end{aligned}
\tag{10}
$$

For our current experimental setup, the external force is provided by a piezoelectric buzzer that spans a 9-mm length along the needle from 2 cm to 2.9 cm, yielding a new form for (12):

$$Q_n(t) = \int_{a=0.02}^{0.029} P_o \sin(\omega_{\text{drive}} t)\, X_n(a)da. \tag{15}$$

To obtain a solution for the transverse motion for this distributed force, we substitute (9) and (15) into (11). This yields the following equation:

$$
\begin{aligned}
w(x,t) = \sum_{n=1}^{\infty} \Bigg[&\int_{a=0.02}^{0.029} X_n(a)da \frac{2P_o}{\rho\Omega L\omega_n} \\
&\times \frac{\omega_{\text{drive}}\sin(\omega_n t) - \omega_n \sin(\omega_{\text{drive}} t)}{\omega_{\text{drive}}^2 - \omega_n^2}\Bigg] X_n(x).
\end{aligned}
\tag{16}
$$

B. Model Simulations

All simulations were coded using MATLAB (Mathworks, Inc., Natick, MA). In the simulations, the needle was sampled every millimeter along its length, the vibrations were temporally sampled at 4.5 kHz to match the pulse repetition frequency (PRF) of the ultrasound system, and the simulations were run over 100 time steps (∼22 ms). Table I shows the material property values for a hollow stainless steel rod that was used for the simulations.

TABLE I
MATERIAL PROPERTY VALUES FOR A HOLLOW STAINLESS STEEL ROD AND UNITS USED FOR THE MODEL SIMULATIONS.

Property	Value	Units
Density (ρ)	7800	kg/m^3
Cross-sectional area (Ω)	5.2×10^{-7}	m^2
Young's modulus (E)	193×10^9	Pa
Radius of gyration (κ)	2.03×10^{-4}	m
Speed of sound (c)	5e3	m/s
Length (L)	0.66	m
Force amplitude (P_o)	0.001	N

C. Ultrasound Experiments

To validate our model, a series of water tank experiments were performed to measure the vibrations along the length of the needle. The Volumetrics Model 1 3-D ultrasound system described earlier was used to acquire the echo data for these experiments. A custom designed transesophageal ultrasound probe capable of acquiring 3-D echo, 3-D color Doppler, and 3-D PW spectral Doppler scanning was used. This probe has been described in detail by Pua *et al.* [16].

The ultrasound system's PW spectral Doppler option was used to detect the nodes and antinodes of the vibrating septal puncture needle. Although capable of 3-D PW spectral Doppler, the system was used to measure vibrations in one dimension along a single image plane for these experiments. Figs. 3(A) and (B) are orthogonal slices showing

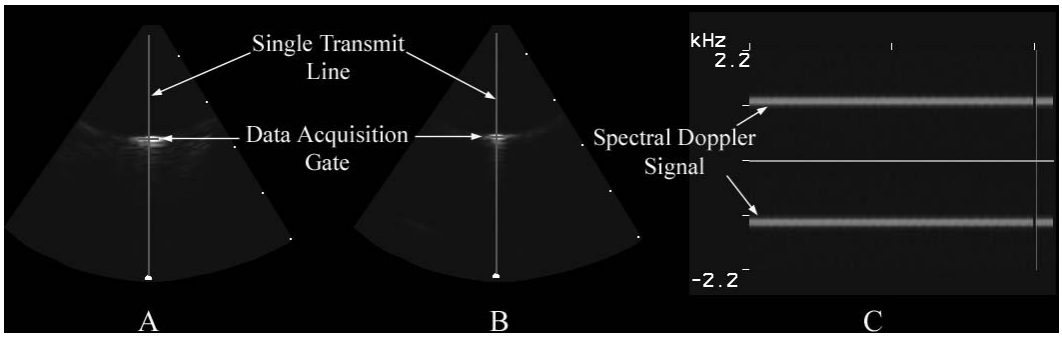

Fig. 3. Example set of spectral Doppler images. (A) is a B-scan image slice showing the needle in long axis. The line down the middle represents the single echo line for spectral Doppler processing. The horizontal line represent the acquisition range gate. (B) is the orthogonal B-scan image slice showing the needle in short axis, again with the spectral Doppler line and acquisition range gate present. (C) shows the display of the frequency spectral data plotted against time. The intensity at a particular frequency and time signifies signal strength.

the needle in long axis and short axis views. The vertical line indicates the 3-D scan line. The horizontal line shows the acquisition range gate used for the spectral Doppler. For our experiments, the acquisition range gate was set to the minimum width, which causes data acquisition at a single depth location. To obtain the processed PW spectral Doppler signal [Fig. 3(C)], the returned echo signal is high pass filtered (wall filtered) to remove the stationary echoes, leaving the oscillating signal. Next, the scanner performs a 256-point fast Fourier transform (FFT) that yields the frequency spectrum of the data. The processed data then is shown as a linear display with the frequency on the y-axis and time on the x-axis. The brightness of the signal at a specific point on the screen is proportional to the amplitude of the frequency spectra at a particular time [17]. An algorithm similar to this PW spectral Doppler processing was coded in MATLAB so that the model vibration data could be processed in the same manner to compare the experimental results to the simulation data.

The nodes and antinodes of the vibrating needle were found experimentally by acquiring PW Doppler data along the length of the needle, with the first data point acquired at the tip and subsequent data acquired every 2 mm after that for 10 cm. Images of the ultrasound system's display were captured for each data point location. The PW spectral Doppler maximum signal strength value and the frequency for the processed data then were found by using MATLAB to detect the maximum brightness value associated with the frequency spectrum.

III. Results

Fig. 4 shows the plots for the free vibrations for the 18th mode, which in our case corresponds to a vibration frequency of 1.115 kHz. This frequency was considered because it was found to work very well for the needle experiments previously described [10]. Referring to Fig. 4, one can see that the first antinode is found at 2.69 cm and the first node (not including the fixed end) appears at 4.74 cm, with both locations denoted by the dashed lines in the figure. This information can be used to help

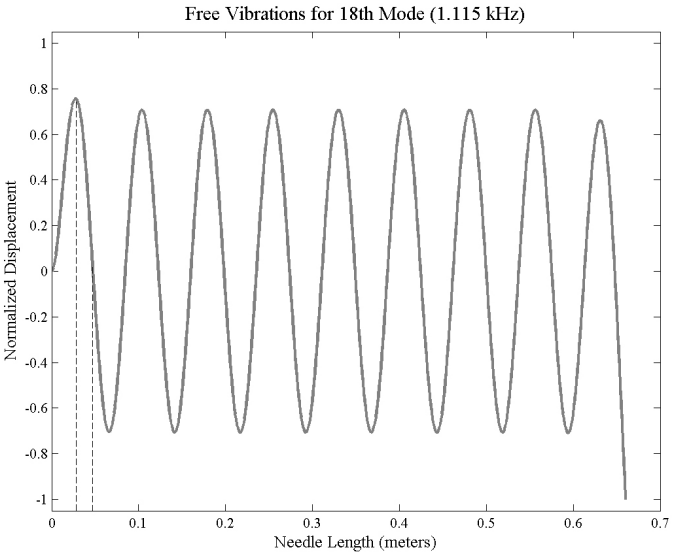

Fig. 4. Free vibrations along the needle length for the 18th mode. The first natural antinode (2.69 cm) and node (4.74 cm) are marked by the dashed lines.

determine the appropriate location to apply the forced vibration. The antinodes are the desirable driving points because they result in the largest tip deflections. In Fig. 4, the free end tip of the device is displaced more than the rest of the antinodes along the needle in all of the plots. This is a direct result of the beam wave equation (1) containing the fourth derivative function with respect to x. This is in contrast to the traditional vibrating string wave equation $((\partial^2 y/\partial x^2) = (\rho/E)(\partial^2 y/\partial t^2))$ [15], in which the free end antinode displaces the same distance as all other antinodes.

To find a relationship between the vibration mode and the natural nodes, the location of the first five nodes (when applicable) were found for the first 12 modes of vibration. Using these locations, the following relationship was developed to locate the natural nodes:

$$\text{node location} = L * \left((0.2992 + (1.1744 * nn)) * vm^{-1.0473}\right), \quad (17)$$

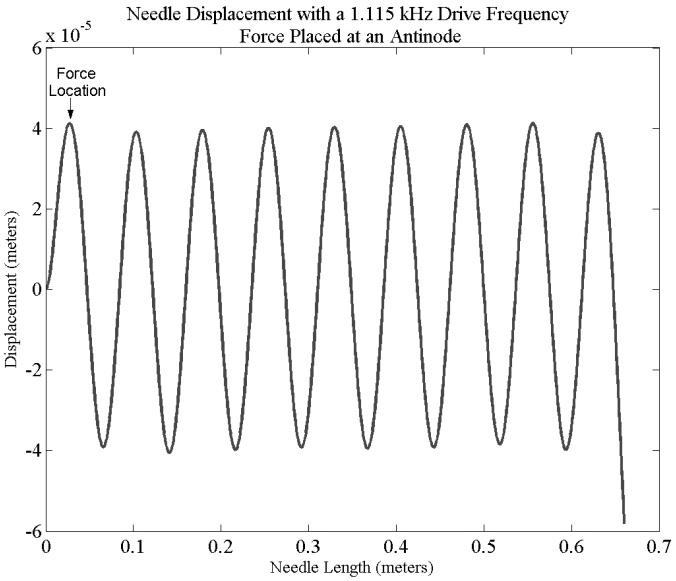

Fig. 5. Forced vibration along the needle length with force applied at the antinode ($x = 2.69$ cm).

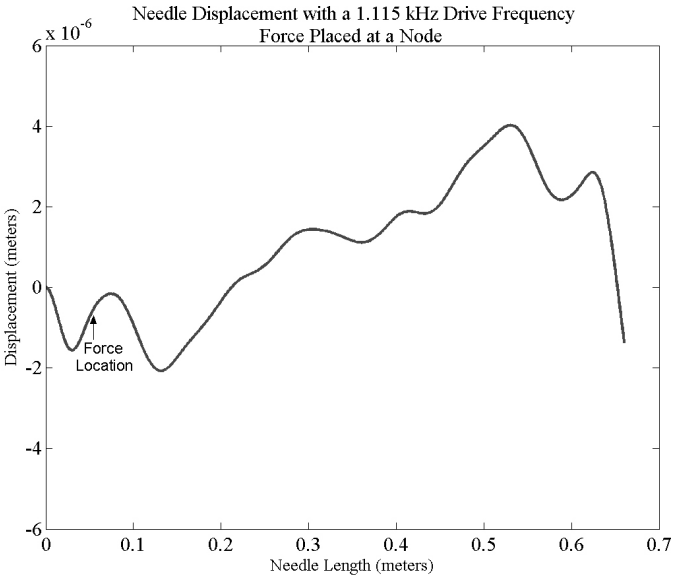

Fig. 6. Forced vibration along the needle length with force applied at the node ($x = 4.74$ cm).

where L is the device length, vm is the vibration mode of interest, nn is the desired node, counted from the fixed end. The fixed end is not included in this count. This relationship can be used to estimate the nodal period of the device for a particular vibration mode (i.e., drive frequency).

As an illustrative example, the time-varying sinusoidal forcing function was placed at an antinode and a node in the MATLAB simulation based on (14). The resulting vibrations at a particular time point are shown in Figs. 5 and 6, respectively. Comparing these figures, one can see an order of magnitude increase in vibration amplitude when the forcing function is placed at antinode compared to the node placement.

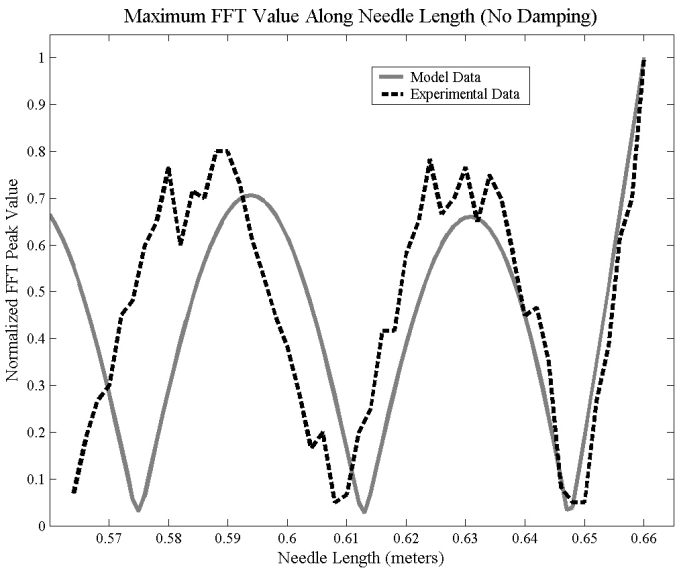

Fig. 7. Comparing the simulation displacements to those collected using the ultrasound system. The data shows the FFT of the returned displacements along the needle length. The FFT values are normalized for the comparison.

Our current experimental setup includes a straight needle, length 66 cm, and a time-varying sinusoidal forcing function ($f_{\text{drive}} = 1.115$ kHz) is generated by attaching a piezoelectric buzzer to the needle. The attachment point for the buzzer spans a range that starts 2 cm from the fixed end and ends at 2.9 cm away from the fixed end. Fig. 7 shows the comparison of the experimental spectral Doppler data (dotted line) and the calculated FFT model data (solid line) using the transverse displacement data from (16) for the distributed force case. The y-axis shows the normalized frequency spectrum maximum value, and the x-axis is the needle length, with the free end at the right. The model data agrees with the experimental data for the initial 5 cm distance from the tip. Further model improvements are discussed below.

IV. Discussion

Our initial experiments in tracking vibrating devices [10] showed promising results, but there was still a need to improve our design to increase the SNR of the tip deflection. We believe that increasing the tip deflections may address the reliability and consistency issues observed during our earlier experiments. As a first step toward increasing the tip deflection, we have developed an analytical model that models the experimental vibrations of a straight needle in a water tank. Knowing the location of the nodes and antinodes is critical for improving vibration efficiency along the needle. We now can apply the forcing function at an antinode to achieve maximum deflections along the needle, especially at the tip.

In our initial results, we can see that the experimental data and the model data match for the first 5 cm (Fig. 7). The cause of the discrepancy after the initial 5 cm

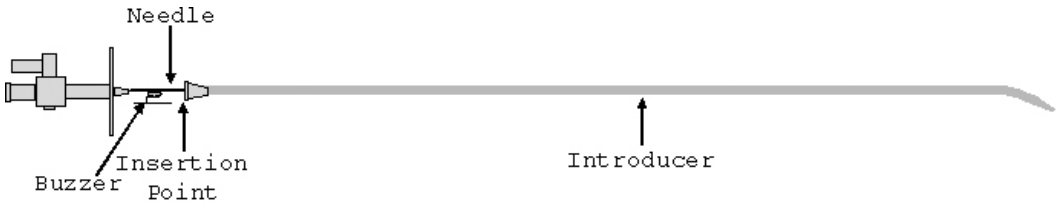

Fig. 8. Schematic of the needle within the introducer catheter for clinical applications. The model will be used to create a node at the insertion point to ensure vibrations are able to reach the tip.

is thought to be the damping effects caused by the water surrounding the vibrating needle in the experiments. To account for the damping, one may consider adding a velocity damping term to (1). From our experiments, the needle vibrating velocity is typically in the range of 10–80 cm/s, which leads to the assumption that viscous damping is the predominate damping [15]. The new equation of motion then would be:

$$EI\frac{\partial^4 w(x,t)}{\partial x^4} = p(x,t) - \rho\Omega\frac{\partial^2 w(x,t)}{\partial t^2} - d\frac{\partial w(x,t)}{\partial t}. \quad (18)$$

This equation can be solved as before using separation of variables, as done previously in Section II. The characteristic equation would remain the same because the additional damping term in (18) is time dependent. In order to solve this equation, the viscous damping coefficient d needs to be characterized.

Our current model considers only motion in a 1-D transverse plane; however, it is likely that there is movement in more than a single plane. Modeling the system in more than one dimension could improve our characterization of the vibrating system. There are several other additions that we can add to improve our model, including a distributed load along the needle length to compensate for gravity effects and incorporating more complex geometries to more accurately model the device.

V. Conclusions

In clinical use, an atrial septal puncture needle is inserted into the body and guided to the right atrium while within an introducer catheter (Fig. 8) [18]. With the model described above, we can use a drive frequency that will create a node at the insertion point where the needle enters the introducer. This will ensure that the vibrations are not suppressed near the proximal end, permitting vibrations to travel along the needle to the free end of the device that is being monitored by our Doppler tracking technique.

References

[1] W. C. Culp, T. C. McCowan, T. C. Goertzen, T. G. Habbe, M. M. Hummel, R. F. LeVeen, and J. C. Anderson, "Relative ultrasonographic echogenicity of standard, dimpled, and polymeric-coated needles," *J. Vascu. Intervent. Radiol.*, vol. 11, pp. 351–358, 2000.

[2] S. Gupta, "New techniques in image-guided percutaneous biopsy," *Cardiovascu. Intervent. Radiol.*, vol. 27, pp. 91–104, 2004.

[3] R. E. Hopkins and M. Bradley, "In-vitro visualization of biopsy needles with ultrasound: A comparative study of standard and echogenic needles using an ultrasound phantom," *Clin. Radiol.*, vol. 56, pp. 499–502, 2001.

[4] D. I. Jandzinski, N. Carson, D. Davis, D. J. Rubens, S. L. Voci, and R. H. Gottlieb, "Treated needles—Do they facilitate sonographically guided biopsies?," *J. Ultrasound Med.*, vol. 22, pp. 1233–1237, 2003.

[5] D. Vilkomerson and D. Lyons, "A system for ultrasonic beacon-guidance of catheters and other minimally-invasive medical devices," *IEEE Trans. Ultrason., Ferroelect., Freq. Contr.*, vol. 44, pp. 496–504, 1997.

[6] D. Vilkomerson and D. Lyons, "A system for ultrasonic beacon-guidance of catheters and other minimally-invasive medical devices," *IEEE Trans. Ultrason., Ferroelect., Freq. Contr.*, vol. 44, pp. 27–35, 1997.

[7] C. L. Merdes and P. D. Wolf, "Locating a catheter transducer in a three-dimensional ultrasound imaging field," *IEEE Trans. Biomed. Eng.*, vol. 48, pp. 1444–1452, 2001.

[8] M. Gorguner, F. Misirlioglu, P. Polat, H. Kaynar, L. Saglam, A. Mirici, and S. Suma, "Color Doppler sonographically guided transthoracic needle aspiration of lung and mediastinal masses," *J. Ultrasound Med.*, vol. 22, pp. 703–708, 2003.

[9] G. Armstrong, L. Cardon, D. Vilkomerson, D. Lipson, J. Wong, L. L. Rodriguez, J. D. Thomas, and B. P. Griffin, "Localization of needle tip with color Doppler during pericardiocentesis: In vitro validation and initial clinical application," *J. Amer. Soc. Echocardio.*, vol. 14, pp. 29–37, 2001.

[10] M. P. Fronheiser, P. D. Wolf, S. F. Idriss, R. C. Nelson, W. Lee, and S. W. Smith, "Real-time 3-D color flow Doppler for guidance of vibrating interventional devices," *Ultrason. Imag.*, vol. 26, pp. 173–184, 2004.

[11] S. W. Smith, R. C. Booi, E. D. Light, C. L. Merdes, and P. D. Wolf, "Guidance of cardiac pacemaker leads using real time 3D ultrasound: Feasibility studies," *Ultrason. Imag.*, vol. 24, pp. 119–128, 2002.

[12] S. W. Smith, H. G. Pavy, and O. T. von Ramm, "High-speed ultrasound volumetric imaging-system 1. Transducer design and beam steering," *IEEE Trans. Ultrason., Ferroelect., Freq. Contr.*, vol. 38, pp. 100–108, 1991.

[13] O. T. von Ramm, S. W. Smith, and H. G. Pavy, "High-speed ultrasound volumetric imaging-system 2. Parallel processing and image display," *IEEE Trans. Ultrason., Ferroelect., Freq. Contr.*, vol. 38, pp. 109–115, 1991.

[14] B. Gardineer and J. W. Bogan, "Drive apparatus for an interventional medical device used in an ultrasonic imaging system," U.S. Patent 5,967,991, Oct. 19, 1999.

[15] E. Volterra and E. C. Zachmanoglou, *Dynamics of Vibrations.* Columbus, OH: Charles E. Merrill Books, 1965.

[16] E. C. Pua, S. F. Idriss, P. D. Wolf, and S. W. Smith, "Real-time 3-D transesophageal echocardiography," *Ultrason. Imag.*, vol. 26, pp. 217–232, 2004.

[17] J. A. Jensen, *Estimation of Blood Velocities Using Ultrasound: A Signal Processing Approach.* Cambridge: Cambridge Univ. Press, 1996.

[18] E. C. Brockenbrough and E. Braunwald, "A new technique for left ventricular angiocardiography and transseptal left heart catheterization," *Amer. J. Cardiol.*, vol. 6, pp. 1062–1064, 1960.

Matthew P. Fronheiser was born in Pottstown, PA, on January 13, 1980. He received a B.S. degree in biomedical engineering from the Catholic University of America, Washington, DC, in 2002.

Currently, he is a biomedical engineering doctoral candidate at Duke University, Durham, NC. His current research focuses on the guidance of interventional devices during minimally invasive surgery using real-time volumetric imaging.

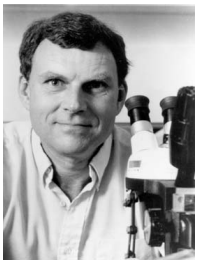

Stephen W. Smith (M'91) was born in Covington, KY, on July 27, 1947. He received the B.A. degree in physics (summa cum laude) in 1967 from Thomas More College, Ft. Mitchell, KY, the M.S. degree in physics in 1969 from Iowa State University, Ames, and the Ph.D. degree in biomedical engineering in 1975 from Duke University, Durham, NC.

In 1969, he became a Commissioned Officer in the U.S. Public Health Service, assigned to the Food and Drug Administration, Center for Devices and Radiological Health, Rockville, MD, where he worked until 1990 in the study of medical imaging, particularly diagnostic ultrasound and in the development of performance standards for such equipment. In 1978, he became an adjunct associate professor of radiology at Duke University Medical Center. In 1990, he became an associate professor of biomedical engineering and radiology, and Director of Undergraduate Studies in Biomedical Engineering at Duke University. He holds 16 patents in medical ultrasound and has authored 100+ publications in the field.

Dr. Smith is cofounder of Volumetrics Medical Imaging. He has served on the education committee of the American Institute of Ultrasound in Medicine, the executive board of the American Registry of Diagnostic Medical Sonographers, the editorial board of *Ultrasonic Imaging*, and the Technical Program Committee of IEEE-UFFC. He was corecipient of the American Institute of Ultrasound in Medicine Matzuk Award in 1988 and 1990 and corecipient of the IEEE-UFFC Outstanding Paper Award in 1983 and 1994.